PNAS RESEARCH ARTICLE | PHYSIOLOGY

# Essential role of N-terminal SAM regions in STIM1 multimerization and function

Matthias Sallinger[a], Christina Humer[a], Hwei Ling Ong[b], Sasirekha Narayanasamy[b], Qi Tong Lin[c], Marc Fahrner[a], Herwig Grabmayr[a], Sascha Berlansky[a], Sean Choi[b], Tony Schmidt[d], Lena Maltan[a], Lara Atzgerstorfer[a], Martin Niederwieser[d], Irene Frischauf[a], Christoph Romanin[a], Peter B. Stathopulos[c], Indu Ambudkar[b], Romana Leitner[a], Daniel Bonhenry[e,1], and Rainer Schindl[d,1]

Edited by Mohamed Trebak, University of Pittsburgh, Pittsburgh, PA; received November 15, 2023; accepted April 11, 2024 by Editorial Board Member Mark T. Nelson

**The single-pass transmembrane protein Stromal Interaction Molecule 1 (STIM1), located in the endoplasmic reticulum (ER) membrane, possesses two main functions: It senses the ER-$Ca^{2+}$ concentration and directly binds to the store-operated $Ca^{2+}$ channel Orai1 for its activation when $Ca^{2+}$ recedes. At high resting ER-$Ca^{2+}$ concentration, the ER-luminal STIM1 domain is kept monomeric but undergoes di/multimerization once stores are depleted. Luminal STIM1 multimerization is essential to unleash the STIM C-terminal binding site for Orai1 channels. However, structural basis of the luminal association sites has so far been elusive. Here, we employed molecular dynamics (MD) simulations and identified two essential di/multimerization segments, the α7 and the adjacent region near the α9-helix in the sterile alpha motif (SAM) domain. Based on MD results, we targeted the two STIM1 SAM domains by engineering point mutations. These mutations interfered with higher-order multimerization of ER-luminal fragments in biochemical assays and puncta formation in live-cell experiments upon $Ca^{2+}$ store depletion. The STIM1 multimerization impeded mutants significantly reduced $Ca^{2+}$ entry via Orai1, decreasing the $Ca^{2+}$ oscillation frequency as well as store-operated $Ca^{2+}$ entry. Combination of the ER-luminal STIM1 multimerization mutations with gain of function mutations and coexpression of Orai1 partially ameliorated functional defects. Our data point to a hydrophobicity-driven binding within the ER-luminal STIM1 multimer that needs to switch between resting monomeric and activated multimeric state. Altogether, these data reveal that interactions between SAM domains of STIM1 monomers are critical for multimerization and activation of the protein.**

STIM | EF-SAM | SOCE | Orai

## Significance

In this study, we unravel the elusive endoplasmic reticulum (ER)-luminal multimerization region of Stromal Interaction Molecule 1 (STIM1), a pivotal regulator of store-operated calcium homeostasis. Using molecular dynamics simulations, we pinpoint two critical multimerization segments within the STIM1 sterile alpha motif (SAM) domain. Through engineered point mutations, we disrupt STIM1 SAM multimerization, impeding ER-luminal fragment multimerization and subsequent Orai1 channel activation. This disruption leads to diminished STIM1 puncta formation and decreased oscillatory calcium patterns, emphasizing the essential role of the STIM1 multimerization regions in orchestrating store-operated calcium channel activation. Our findings shed light on the hydrophobicity-driven dynamics underlying STIM1 multimerization, providing crucial insights into calcium signaling regulation.

Rises in cytosolic calcium ($Ca^{2+}$) play a ubiquitous role as second messengers, enabling versatile cellular signaling (1, 2). One mechanism to generate local cytosolic $Ca^{2+}$ signals and global $Ca^{2+}$ oscillations is the store-operated $Ca^{2+}$ entry (SOCE) pathway, which links endoplasmic reticulum (ER) $Ca^{2+}$ store depletion to $Ca^{2+}$ influx from the extracellular space (3–5). SOCE is crucial for diverse functions on a cellular and organismal level, including transcription factor activation, secretion, and immunological defense (1–3, 5). The $Ca^{2+}$ sensing proteins, Stromal Interaction Molecule (STIM) 1 and STIM2 located in the ER-membrane, together with the plasma membrane (PM) $Ca^{2+}$ channels Orai1, 2, and 3 are the major components of the SOCE family (6–13). Assemblies of ER-resident STIM and PM-located Orai channels compose the $Ca^{2+}$ release-activated $Ca^{2+}$ (CRAC) channel complex, activated via signaling cascades that reduce the ER-luminal $Ca^{2+}$ concentration from around 800 μM at rest to 100-400 μM (14). STIM1 acts as a precise $Ca^{2+}$ sensor, dynamically moving along microtubules under high $[Ca^{2+}]_{ER}$ resting state conditions. When ER-$Ca^{2+}$ stores get depleted, STIM1 loses bound $Ca^{2+}$ from the ER-luminal domain and redistributes into so-called puncta at ER-PM junctions, where physical interaction between STIM and Orai proteins leads to an influx of $Ca^{2+}$ across the PM (11, 15–18).

The N-terminal, ER-lumen facing parts of all STIM proteins contain three highly conserved structural segments: a canonical EF-hand (cEF) domain that enables $Ca^{2+}$ sensing, a stabilizing noncanonical EF-hand (nEF) domain, and a sterile α-motif (SAM). The ER-luminal part is connected to a series of C-terminal, cytosolic coiled-coil (CC) domains via a single pass α-helical transmembrane (TM) domain (19–22). STIM1 adopts dimeric assemblies under resting cell conditions, held together by intermolecular interactions via the C-terminal CRAC activating domain (CAD), also named the STIM1 Orai activating region (SOAR) (18, 23–27). While overall dimeric, high-resolution NMR data and X-ray crystal structures revealed that the N termini of *human* STIM1,

The authors declare no competing interest.

This article is a PNAS Direct Submission. M.T. is a guest editor invited by the Editorial Board.



[1]To whom correspondence may be addressed. Email: daniel.bonhenry@uni.lu or rainer.schindl@medunigraz.at.

This article contains supporting information online at https://www.pnas.org/lookup/suppl/doi:10.1073/pnas.2318874121/-/DCSupplemental.

Published May 16, 2024.

*human* STIM2, and *Caenorhabditis elegans* (*C. elegans*) STIM are kept in a monomeric state under high $Ca^{2+}$ concentration (20–22). These structures show 10 common α-helices and two short β-strands, with the EF-hand domains having four α-helices (α1 to 4) and two loops connected via a short helix (α5) to the SAM domain, the latter of which is made out of a five-helix bundle (α6 to 10). Binding of $Ca^{2+}$ to the EF-hand domain is important to keep the ER-luminal STIM1 structure in a well-folded, compact conformation (22). All three domains, the $Ca^{2+}$-bound cEF-hand, nEF-hand together with the SAM domain, are important for maintaining this compact conformation based on intramolecular interactions, which give rise to a hydrophobic central core (17, 22). In addition, negatively charged residues on the surface of this structure likely prevent the N terminus from intermolecular dimerization during resting cell conditions (20–22). Remarkably, the high-resolution structures of resting state *h*STIM1, *h*STIM2, and *C. elegans* STIM reveal differences in the compact packaging between the two EF hands and the SAM domain, respectively, owning important consequences on function (20–22). Considering the latter, the precise multimerization of these three domains determines both $Ca^{2+}$ binding affinity and dynamics upon $Ca^{2+}$ depletion-induced protein activation (20–22, 28–34). Subsequent critical activation steps, including a coiled-coil zipping process that induces a large conformational change in the C-terminal part of STIM1 to unleash CAD for Orai1 binding together with puncta formation, require interaction(s) between luminal STIM1 domains (21, 22, 35–38). How ER-luminal STIM1 domains bind to each other to form multimers upon $Ca^{2+}$ store depletion remains structurally elusive so far.

To address this, we hypothesized that molecular dynamics (MD) simulations on the available high-resolution structure of ER-luminal *h*STIM1 could allow for the identification of structural features of ER-$Ca^{2+}$ store depletion–associated multimerization. Importantly, previous work has determined a structural correlation of NMR with an MD simulation-based approach. At low $Ca^{2+}$ conditions, NMR experiments revealed a conformational exchange of an ancillary α-helix (α0), unfolding of two EF-hand helices (α2-α3) together with an α-helix to beta-strand transition at the C-terminal end of *C. elegans* STIM EF-SAM domain (20). Our MD simulations showed that the unfolding of these two *h*STIM1 EF-hand domain helices is remarkably similar to previously determined *C. elegans* STIM NMR results. Still, besides unfolding of these two α-helices, the overall luminal STIM1 structure remained structured in MD simulations (30, 31). Out of the α1 to α3 region, the backbone residues of α1 were assigned for *C. elegans* STIM in low $Ca^{2+}$, supporting the notion that the poor dispersion/chemical exchange observed for α2 and α3 is also associated with unfolding of the two helices (20, 30, 31). In accordance, a recently published temperature-driven MD approach also reported that the cEF-hand domain helices destabilized upon $Ca^{2+}$ depletion, whereas at physiological temperature the nEF-hand is predominantly destabilized, while the SAM domain remained stable, determining striking similarities to $Ca^{2+}$ depletion structures of our work (30, 31, 39). The MD simulations in our and other publications determined that upon $Ca^{2+}$ depletion the overall luminal STIM1 structure remained structured besides extension of the $Ca^{2+}$ binding region.

In this work, we first monitored ER-luminal *h*STIM1 dimerization using MD simulations to determine residues within the STIM1 SAM domain essential for luminal di/multimerization. Engineered point mutations significantly abolished STIM1 cluster formation and SOCE.

## Results

**MD Simulations Reveal Frequent Intermolecular Contacts of $Ca^{2+}$-Unbound ER-Luminal STIM1.** As a starting point, we based our MD simulation approach on the high-resolution NMR structure of the compactly folded *h*STIM1 N-terminal EF-SAM domain (aa58-201, PDB:2K60) in $Ca^{2+}$-bound conditions (Fig. 1*A*) (22). This structure was linked with a rebuilt transmembrane (TM) α-helix, the latter of which was embedded in a 1-palmitoyl-2-oleoyl-glycero-3-phosphocholine (POPC) lipid bilayer. In addition, this domain was linked with a CC1-α1 region that exhibited a continuous α-helix (aa202 to 271) (*SI Appendix*, Fig. S1*A*) (40). Hence, the simulated STIM1 largely resembled STIM1 with a truncation before CAD. Simulations of two identical STIM1 monomers were started using three different orientations. Specifically, the EF hands and SAM domains were placed in close proximity (>5Å) in an environment containing a high $Ca^{2+}$ concentration of 0.1 M $CaCl_2$ (*SI Appendix*, Fig. S1*A*). To investigate residue-contact sites occurring during the simulation time of 200 ns, distances between the $C_\alpha$ atoms of residues in one monomer and the $C_\alpha$ atoms of other monomer residues, were calculated and contacts were counted with a cutoff radius below 10Å (Fig. 1*C*, black bars). The formed contact counts are summed up from three different starting configurations each simulated in duplicates. As each monomer was able to move freely in the membrane, transient interactions between folded luminal STIM1 monomers occurred (Fig. 1*C*, black bars). While interactions between folded monomers were located in the nEF-hand domain and SAM domain, these occurred as transient nonstable contacts, as the EF-SAM domain remained in a compactly folded conformation (Fig. 1*C*, black bars).

In an analogous approach, we simulated the dimerization of $Ca^{2+}$-free STIM1 that already contained two largely unfolded cEF- and nEF-hand helices, at α2 and α3 of the STIM1 N terminus, at the beginning of the simulation (Fig. 1 *A* and *B* and Movie S1), based on our previous work and in line with 2D-NMR data (22, 30, 31, 39). Again, three different orientations in duplicates were used as starting configurations for MD simulations (*SI Appendix*, Fig. S1*B*). Thereby, $CaCl_2$ was exchanged with 0.15 M KCl to represent $Ca^{2+}$-free conditions (*SI Appendix*, Fig. S1*B*). During the simulations, we observed a prominent increase in the number of contacts when compared to the simulation of the $Ca^{2+}$-bound counterparts (Fig. 1 *B* and *C*, colored bars; Movie S2). The luminal dimer formation as observed in our simulations, involves intact helical structures but also flexible domains (Fig. 1*B*). Specifically, most frequently interacting STIM1 luminal residues were determined in the nEF-hand (aa100-110) together with two regions in the SAM domain (aa150 to 160 and aa175 to 180) (Fig. 1*C*, colored bars). All three segments showed substantially higher contacts than in the respective $Ca^{2+}$-bound STIM1 simulations (Fig. 1*C*, compare black with colored bars). The overall simulated STIM1 dimerization process was a dynamic system formed throughout several intermediate states that is presented at representative MD simulation snapshots at different time-points (Fig. 1*B* and *SI Appendix*, Fig. S1*C* and Movie S2). Highly interacting amino acids involved mainly hydrophobic and positively charged side-chains but also certain neutral/polar side-chains (Fig. 1*C*). Among the identified three potential luminal multimerization sites, the nEF-hand was also shown to be important for stabilization of compact resting configurations forming contact sites with parts of the SAM domain (21, 22, 31, 39). The highest interaction counts within the nEF-hand were identified among residues F108 and H109, which we and others have previously characterized in MD simulations and functional recordings upon introducing distinct point mutations (30, 31, 39).

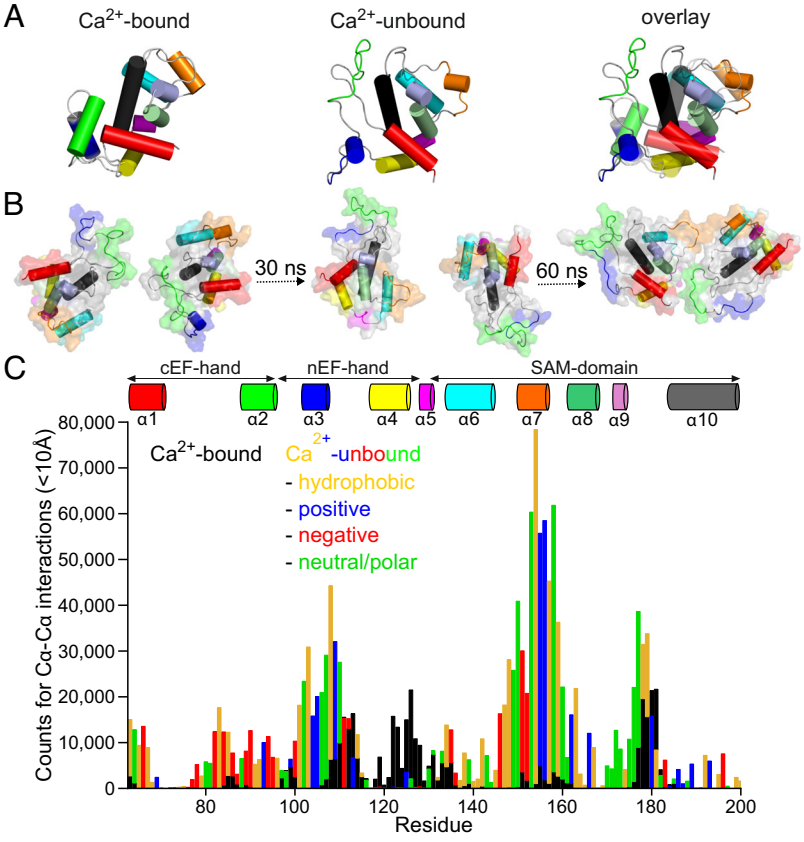


**Fig. 1.** Molecular dynamics simulations of ER-luminal STIM1 dimerization. (*A*) Structural representation of ER-luminal *h*STIM1 [PDB:2K60 (22)] in the $Ca^{2+}$-bound state (*Left*), $Ca^{2+}$ unbound (*Middle*), and their overlay (*Right*) depicted from MD simulations (30, 31). (*B*) Representative MD simulation snapshots of two ER-luminal STIM1 monomers (starting configuration as in a *Middle* image) in 0.15 M KCl environment, after 30 ns and 60 ns simulation time, respectively. (*C*) Histogram of residue–residue contact counts for $Ca^{2+}$-bound (in black) and $Ca^{2+}$-unbound STIM1 (in color code) summarized from three different starting configurations after two simulation runs each. Counts were based on calculated distances between the $C_\alpha$ of a residue in one monomer and the $C_\alpha$ of the residues in the other monomer with a cut-off radius of 10Å during 200 ns simulation time. Helices are represented as cylinders in MD snapshots (*A*) and (*B*) in a color code corresponding to the schematic shown in (*C*).

Single point mutations that disrupt the compactly folded structure of the STIM1 N terminus have been shown to cause severe pathological phenotypes of tubular aggregate myopathy (TAM) and the multisystemic Stormorken syndrome (31, 40–42). In particular, for the TAM disease mutants F108I, H109N, and H109R, it has been shown that constitutive STIM1 activation is triggered through the disturbance of the hydrophobic cleft region, which contains residues from both cEF- and nEF-hand domains further stabilized by the SAM region, giving rise to disease-related phenotypes (22, 30, 31, 41). In contrast to the nEF-hand domain, the highest counts for two regions in the SAM domain segments (aa150 to 160 and aa175 to 180) have not been characterized before. Thus, we focused on these segments as important regions for luminal STIM1 di/multimerization.

**Identification of SAM Residues That Form Frequent Luminal STIM1–STIM1 Interactions.** To understand which residues of the SAM region are essential for di/multimerization of STIM1, we focused on the highest count rates determined in our MD simulations. Two prominent peaks were visible in the SAM domain, located at α-helix 7 (α7) and in the adjacent region near the α9-helix (here named: α9) (Fig. 1*C*, colored bars) respectively. Within α7, we identified the highest calculated count value for the hydrophobic residue F154, which was therefore characterized in more detail together with the two highly interacting positively charged residues R155 and K156 that follow in sequence right after the phenylalanine. For the second identified peak in α9, we focused on two hydrophobic residues, V178 and L179 (Fig. 1*C*, colored bars).

As our objective was to determine specific intermolecular amino acid contact sites that contribute to di/multimerization, we specifically analyzed the intermolecular residue–residue interactions for the selected residues (F154, R155, K156, V178, and L179) that occurred during the simulations in $Ca^{2+}$-bound (Fig. 2 *A*, *Left*) and $Ca^{2+}$-unbound conditions (Fig. 2 *A*, *Right*). Calculations of interacting residues were performed using a cutoff radius of 3Å from one residue to the other [interactions occurring for one monomer in orange (monomer A) and for the second monomer in green (monomer B)]. During $Ca^{2+}$-bound folded conditions, few contact sites with low count rates (<2,000) for F154, R155, and K156 and for V178 together with L179 could be identified (Fig. 2 *A*, *Left*). Under $Ca^{2+}$-unbound conditions, we observed several interacting residues with high count rates (>4,000) (Fig. 2 *A*, *Right*). The most frequently interacting residues were located in partially unstructured segments of the SAM domains (Fig. 1*C*, colored bars, Fig. 2 *A*, *Right*, 2*B*). Local hotspots for interactions between α7 residues could be identified with residues in or close to α6, α7, and α9, respectively (E146, L147, P148, Y150, T175, G176, and T177) (Fig. 2 *B*, *Left*). In addition, the hydrophobic residues of α9 showed the highest interactions with α7 (Y150, L157, Q158, and L159) (Fig. 2 *B*, *Right*). We extended one simulation run to 500 ns and observed that these residues remained the most frequent interaction sites. (*SI Appendix*, Fig. S1*C*). Still, we cannot exclude that further prolonged MD simulations would identify further highly interacting amino acids or would capture a final stable dimer formation. The simulations showed that different residues were forming contacts between STIM1 monomers, suggesting that ER luminal di/multimerization contact sites are mainly nonsymmetrical.

These interactions between two SAM domains appeared to be not stabilized by single residue–residue interactions during the simulations but instead, were enabled by dynamic hydrophobic and electrostatic surface properties induced by residues including F154, R155, K156, V178, and L179 that show not only most pronounced count numbers during simulations but also high conservation among species (Fig. 1*C* and *SI Appendix*, Fig. S2 *A*

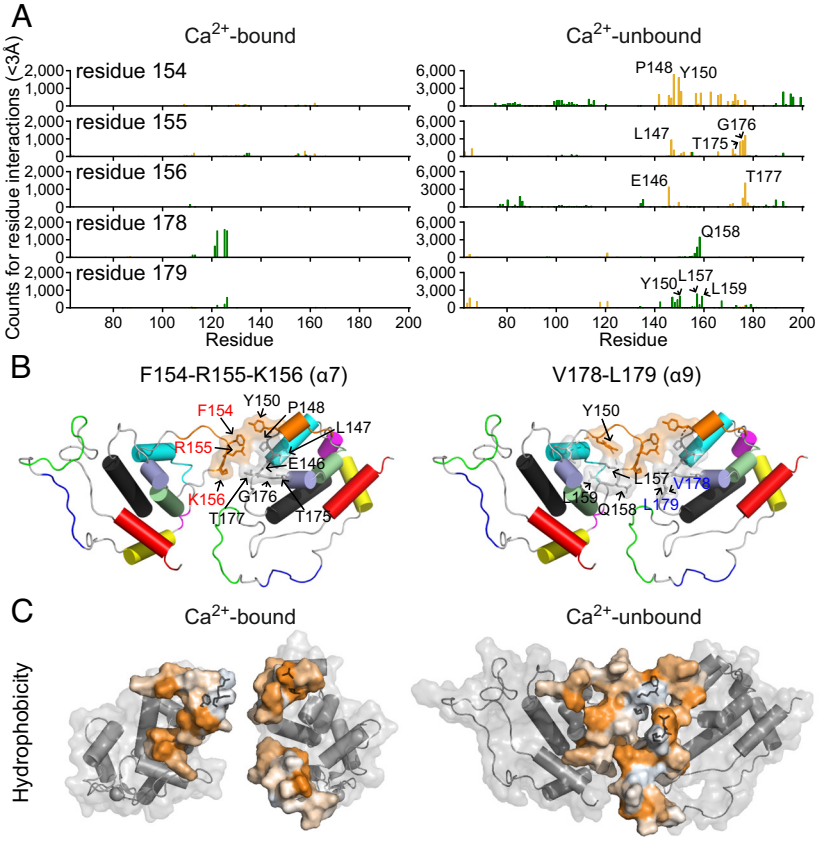


**Fig. 2.** Identification of luminal STIM1 multimerization sites. (*A*) Histogram of residues intermolecular interactions (monomer A in orange and monomer B in green) with a cut-off radius of 3Å during 200 ns simulation time, specifically focused on F154, R155, K156 (in α7), and V178, L179 (the adjacent region near α9) for MD simulations as in Fig. 1*C* for $Ca^{2+}$ bound (*Left*) and $Ca^{2+}$-unbound (*Right*) STIM1 simulations. (*B*) Representative MD simulation snapshots of preferential residue–residue contact sites including F154, R155, K156 (*Left*), and V178 and L179 (*Right*). (*C*) Hydrophobic surface representation of two $Ca^{2+}$ bound STIM1 monomers (*Left*) and $Ca^{2+}$-unbound STIM1 dimer (*Right*) with residues F154, R155, and K156 highlighted in both cases in the left monomer and V178, L179 in the right monomer. Graduating hydrophobicity is represented in different color intensities (dark high, bright low).

and *B* and Movie S2). We visualized the hydrophobic and electrostatic surfaces of the luminal STIM1–STIM1 interactions and highlighted depicted amino acids in comparison to a pair of folded, $Ca^{2+}$-bound STIM1 monomers (Fig. 2*C* and *SI Appendix*, Fig. S2*A*). While $Ca^{2+}$-bound STIM1 showed a highly negatively charged EF-hand surface (*SI Appendix*, Fig. S2*A*; neglecting compensation by positively charged $Ca^{2+}$) with hydrophobic residues being mainly buried within the folded structure (Fig. 2*C*, $Ca^{2+}$ bound), structural changes induced by the loss of $Ca^{2+}$ culminate in the exposure of hydrophobic amino acids (Fig. 2*C*, $Ca^{2+}$ unbound). Instead, only a few charged amino acids are present at the dimer association sites during $Ca^{2+}$ unbound conditions (*SI Appendix*, Fig. S2*A*).

In summary, simulations with $Ca^{2+}$ depleted ER-luminal STIM1 corroborate highly frequent interactions between both monomers mainly involving α7, and the adjacent region near α9. Overall, our simulations visualize luminal EF-SAM di/multimerization sites upon $Ca^{2+}$ store depletion, that involve transiently important interactions mainly driven by hydrophobic residues.

**Mutations within α7 and α9 of SAM Diminish STIM1 Puncta Formation.** $Ca^{2+}$ store depletion triggers concerted conformational transitions within STIM1. STIM1 moves along microtubules during unstimulated conditions and depletion of ER-$Ca^{2+}$ induces large, stable STIM1 clusters named puncta (9, 11, 14). To reach this multimerization process, ER-luminal STIM1 interactions induce a zipping process of the cytosolic CC1 domains to unleash CAD for Orai1 binding (26, 35–37, 42–49). We hypothesize that site-directed mutations of the most frequently observed interacting residues of α7 and α9 that mediate luminal dimerization might not only interfere in luminal contacts but could also place constraints on the subsequent STIM1 activation process. Therefore, we monitored the impact of STIM1 di/multimerization mutants on puncta formation with Total Internal Reflection Fluorescence (TIRF) microscopy using N-terminally cyan fluorescent protein (CFP) tagged STIM1 wild-type (WT) and respective mutants. STIM1-WT expressed in HEK293 cells displayed STIM1 characteristic, directed movement along microtubules under resting cell conditions (Movie S3). Treatment with 25 μM Cyclopiazonic acid (CPA), a SERCA pump inhibitor that induces ER-$Ca^{2+}$ store depletion, resulted in stable, immobile puncta formation (Fig. 3*A* and *SI Appendix*, Fig. S2*C* and Movie S3). Furthermore, the total puncta intensity and mean puncta area increased after CPA treatment for STIM1-WT (Fig. 3*B* and *SI Appendix*, Fig. S2*D*). We sought to disrupt luminal multimerization by creating a triple F154A-R155A-K156A alanine mutant, named α7-mutant and a double V178A-L179A alanine mutant, designated as α9-mutant and performed analogous TIRFM experiments like for STIM1-WT. We focused on these five positions given the high contact numbers observed in MD simulations and the assumption of more prominent effects arising upon exchanging large, hydrophobic, or charged side-chains rather than neutral/polar counterparts by alanines.

During resting conditions, directed movement along microtubules could be observed for both mutants, analogous to STIM1-WT (Movies S4 and S5). Intriguingly, after treatment with 25 μM CPA, STIM1-α7-, and STIM1-α9-mutants continued their directed movements with no, or hardly any stable, immobile cluster formation observed (Fig. 3*A* and *SI Appendix*, Fig. S2*C* and Movies S4 and S5). Even when clusters appeared in the TIRF plane during the measurements, they disassembled after a few seconds, indicating that α7- and α9-mutated proteins were largely incapable of forming solid clusters (Movies S4 and S5). Consistent with the largely reduced number of stable clusters, the total puncta intensity together with the mean puncta area did only show marginal increases after CPA treatment for α7- and α9-mutants, in stark contrast to STIM1-WT (Fig. 3*B* and *SI Appendix*, Fig. S2 *C* and *D*). STIM1-WT

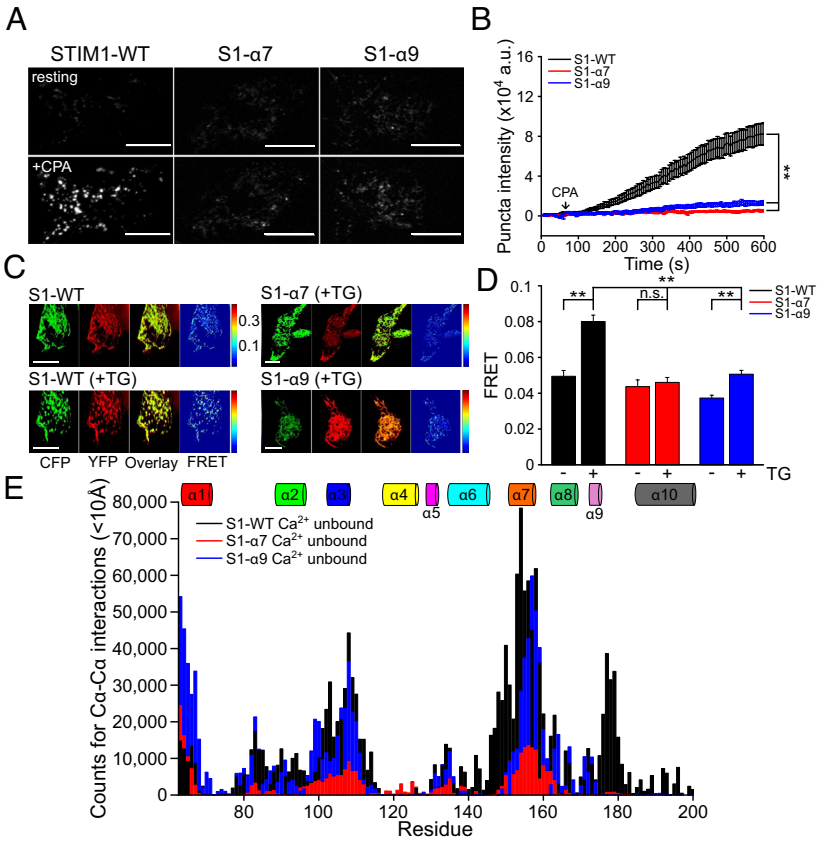


**Fig. 3.** Alanine mutations in α7 and α9 affect STIM1 cluster formation. (*A*) Representative TIRFM images of CFP-tagged STIM1-wild-type (WT), F154A-R155A-K156A (α7), and V178A-L179A (α9) proteins expressed in HEK293 cells. Images were taken at resting state (*Upper*) and after treatment with 25 μM CPA (*Lower*). (*B*) TIRFM data representing total puncta intensity per cell after addition of 25 μM CPA (added at 60 s time point) in 1 mM $Ca^{2+}$ solution for HEK293 cells expressing STIM1-WT (n = 42), STIM1-α7 (n = 30), and STIM1-α9 (n = 35). (*C* and *D*) Representative images of STIM1 homomerization FRET experiments and (*D*) mean values in HEK293 cells expressing C-terminally CFP-/YFP-tagged STIM1-WT (rest: n = 41; TG: n = 62), STIM1-α7 (rest: n = 37; TG: n = 47), and STIM1-α9 (rest: n = 43; TG: n = 58) in response to 1 μM Thapsigargin (TG). (*E*) Histogram of residue–residue contact counts for MD simulations with two STIM1 $Ca^{2+}$-unbound WT forms (in black), STIM1-α7 (in red), and STIM1-α9 (in blue) summarized from three different starting configurations after two simulation runs each. Counts were based on calculated distances between the $C_\alpha$ of a residue in one monomer and the $C_\alpha$ of the residues in the other monomer with a cut-off radius of 10Å during 200 ns simulation time.

and mutants depicted, considering average maximum fluorescence intensity per cell of epifluorescence records, comparable overall expression levels (*SI Appendix*, Fig. S2*E*).

To further address altered STIM1–STIM1 interaction and multimerization after store depletion, we performed STIM1 homomerization Förster-resonance energy transfer (FRET) experiments in HEK293 cells. Consistent with the increasing number of puncta for STIM1-WT after CPA treatment, C-terminally cyan (CFP) and yellow fluorescent protein (YFP) labeled STIM1-WT proteins displayed increasing FRET values after store depletion using 1 μM Thapsigargin (TG), another SERCA inhibitor (Fig. 3 *C* and *D*). Compared to STIM1-WT, the α7- and α9-mutants showed either no or significantly lower increasing FRET after TG treatment (Fig. 3*D*). Analogous experiments of N-terminally tagged STIM1-WT and mutants in S1/S2-double-knock out (dKO) cells, again did not detect any increase in FRET signals compared to STIM1-WT after 1 μM TG treatment. In addition, resting cell FRET values for the α7- and α9-mutants were reduced in comparison to STIM1-WT (*SI Appendix*, Fig. S2 *F* and *G*).

Based on these promising results, we used MD simulations to investigate the dimerization process of $Ca^{2+}$-free STIM1 now with either α7- or α9-point mutants. Within the observation time of 200 ns, neither the α7- nor the α9-mutant impaired the compact SAM domain structure (Movies S6–S8). Clearly, dimerization of the STIM1-α7-mutant was substantially impaired with only occasional dimer contacts. Moreover, the prominent dimerization peaks of STIM1-WT corresponding to α7 and α9 mediated interaction sites, were largely reduced for the α7-mutant (Fig. 3*E* and Movies S6–S8). Dimerization experiments for STIM1-α9 in $Ca^{2+}$-free conditions retained dimer contacts over the simulation time, but the α9 mediated dimer interaction site was largely diminished (Fig. 3*E*).

The results of live-cell experiments, clearly indicate that the substitution of just two (V178A, L179) or three (F154, R155, K156) of the simulation-predicted residues within the identified SAM segments, is sufficient to drastically interfere with STIM1 puncta formation. Intriguingly, a purely computational approach using MD simulations could be used to determine critical residues at α7 and α9 of the SAM domain within the STIM1 luminal multimerization.

**Structural Biology Analysis of Luminal STIM1 α7- and α9-Mutated Peptides.** Next, we evaluated the impact of our identified STIM1 multimerization mutants on $Ca^{2+}$ binding affinity, structural stability, and multimerization ability using recombinantly expressed luminal STIM1 EF-SAM domains (aa58 to 201). *h*STIM1-WT, α7, and α9 EF-SAM-mutant proteins were expressed in *Escherichia coli* (*E. coli*) and purified. Size-exclusion chromatography (SEC) with in-line multiangle light scattering (MALS) was used to assess quaternary structure. The theoretical monomeric molecular weight of STIM1-WT EF-SAM is 17.4 kDa. Consistent with previous work, STIM1-WT EF-SAM eluted primarily as a monomer in the presence of $Ca^{2+}$ with a MALS-determined molecular weight of ~15.4 kDa (*SI Appendix*, Table S1) (21, 22). In the absence of $Ca^{2+}$, luminal STIM1-WT EF-SAM eluted in multiple peaks including dimers (i.e., MALS molecular weights of ~31.6 kDa) and higher-order multimers (Fig. 4*A* and *SI Appendix*, Fig. S3*B* and Table S1). α9-mutated EF-SAM exhibited a WT-like monomeric pattern in $Ca^{2+}$-bound conditions (Fig. 4*C* and *SI Appendix*, Fig. S3*E*). In the absence of $Ca^{2+}$, a transition to preferential multimerization was clearly visible, including dimers (i.e., MALS molecular weight of ~34.1 kDa) however, α9-mutants lacked a prominent peak at an elution volume of ~8 to 12 mL, indicating disruption of these large higher-order multimers that elute close to the column void volume (Fig. 4*C*). Under high $Ca^{2+}$, α7-mutated EF-SAM formed monomers as well as multimers (Fig. 4*B*). The higher-order peaks became more intense concomitant with a decrease in the monomer peak intensity for the α7-mutant in the absence of $Ca^{2+}$ (Fig. 4*B* and *SI Appendix*, Fig. S3*D*). While both mutated proteins were more prone to degradation, as seen on the SDS-PAGE elution

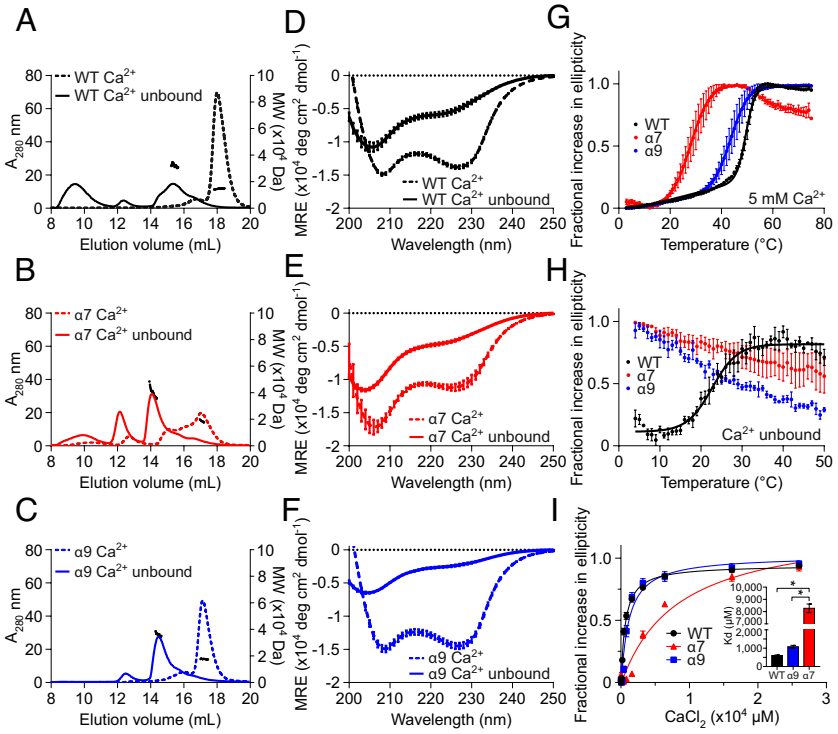


**Fig. 4.** Quaternary, secondary structure, and thermal stability of STIM1 EF-SAM WT, α7-, and α9-mutant. (*A–C*) Representative SEC with in-line MALS data of STIM1-EF-SAM-WT (*A*), α7 (*B*), and α9 (*C*) acquired in the absence (solid line) and presence of 5 mM $CaCl_2$ (dotted line). (*D–F*) Far-UV CD Spectra of STIM1-EF-SAM-WT (*D*), α7 (*E*), α9 (*F*) in the absence (solid line) and presence of $CaCl_2$ (dotted line) acquired at 20 °C. (*G* and *H*) Comparison of the STIM1-EF-SAM-WT and mutants thermal melts based on the fractional change in ellipticity at 225 nm as a function of temperature in the presence (*G*) and absence of $CaCl_2$ (*H*). Far UV-CD spectra were acquired at 20 °C after sequential additions of $CaCl_2$ up to a final concentration of 25 mM. (*I*) The fractional change in ellipticity at 225 nm was plotted versus total divalent cation concentration to construct the binding curves. The equilibrium dissociation constants ($K_d$) were estimated using a one-site binding model that accounts for protein concentration, fit to the data by nonlinear regression. *Inset* shows $K_d$ values for WT, α7-, and α9-mutants.

gels upon $Ca^{2+}$ depletion, the α7-mutation resulted in consistently lower expression/purification yields compared to WT and α9-mutant EF-SAM proteins (i.e., ~30 to 40% of WT) (*SI Appendix*, Fig. S3 *A–F*). We speculate that the α7-mutant could destabilize the EF-hand-SAM domain interaction in the $Ca^{2+}$-loaded state and may point to a double function of α7 that can stabilize both the resting and the multimerization configuration. Comparison of SEC-MALS experiments in $Ca^{2+}$-free conditions between WT, α7, and α9 identified reduced (for α7, Fig. 4*B*) or absent (for α9, Fig. 4*C*) higher-order multimer formation (i.e., elution peak at ~8 to 12 mL) of the mutants (*SI Appendix*, Fig. S3 *B, D,* and *F*). Interestingly, dimer formation seems to remain intact for both mutants (Fig. 4 *A–C*).

To gain a better understanding of $Ca^{2+}$ binding and associated changes in secondary structure of the EF-SAM region in the presence and absence of $Ca^{2+}$, we additionally acquired far-ultraviolet (UV) circular dichroism (CD) spectra. The spectrum of STIM1-WT EF-SAM, measured in the presence of $Ca^{2+}$, showed two minima at ~208 nm and 225 nm, respectively, typical of high levels of α-helicity and as was shown previously (Fig. 4*D*) (21, 22, 30). A similar $Ca^{2+}$-loaded spectrum for the α9-mutant was observed (Fig. 4*F*). In contrast, the α7-mutant EF-SAM showed less negative ellipticity at ~225 nm and a shift of the 208 nm minimum to ~206 nm (Fig. 4*E*), indicating less α-helicity compared to either WT or the α9-mutant. Consistent with the α7-mutations destabilizing the fold in the presence of $Ca^{2+}$, the midpoint of temperature denaturation ($T_m$) was ~22 °C lower compared to WT (Fig. 4 *E* and *G* and *SI Appendix*, Table S1). In contrast, the $T_m$ of α9 only decreased by ~6 °C in comparison to WT under $Ca^{2+}$-bound conditions (Fig. 4*G* and *SI Appendix*, Table S1). In the absence of $Ca^{2+}$, WT EF-SAM unfolded with a $T_m$ of ~23 °C. The dramatic $Ca^{2+}$ depletion-dependent destabilization for WT EF-SAM is congruent with earlier work (21, 22, 30). Interestingly, neither the α7- nor α9-mutant EF-SAM proteins exhibited a thermal unfolding profile in the absence of $Ca^{2+}$ (Fig. 4*H*). Finally, equilibrium dissociation constants ($K_d$) of $Ca^{2+}$ were estimated by monitoring the change in CD ellipticity at 225 nm as a function of increasing $Ca^{2+}$ concentrations. The binding isotherms were fit to a one-site binding model that accounts for protein concentration. Here, the α7-triple-mutant was determined to have a significantly lower $Ca^{2+}$ binding affinity ($K_d$: 8.27 ± 1.65 mM) compared to WT ($K_d$: 0.59 ± 0.05 mM) (Fig. 4*I*). The $K_d$ of the α9-mutant was only slightly lower but not significantly different to WT (Fig. 4*I*).

Together, the EF-SAM structural data highlight that the double-alanine mutation in α9 impairs large, soluble higher-order multimerization when $Ca^{2+}$ is depleted while the impact on the resting/$Ca^{2+}$-loaded state is rather minor. The α7-mutant similarly reduced large, soluble higher-order multimerization compared to WT luminal STIM1 when $Ca^{2+}$ is depleted but also showed multimerization and a marked destabilization even in the presence of $Ca^{2+}$. The effects caused by mutated α7 may be related to the diminished $Ca^{2+}$ binding affinity possibly induced via destabilization of the EF-SAM structure, in line with a double role of SAM in stabilizing both resting and activated/multimerized states.

In an alternative approach to test di/multimerization of luminal STIM1 peptides, we truncated heterologously expressed STIM1 constructs after the TM helix and directly attached CFP or YFP on the cytosolic side of the TM domain (STIM1-Nterm-CFP/YFP) (*SI Appendix*, Fig. S4*A*) to enable both, determination of protein localization and FRET-based interaction analysis in living cellular systems, respectively. When expressed in S1/S2 dKO cells, we observed reticular ER-localized distribution for N-terminal STIM1-WT, α7-, and α9-mutants during resting state conditions (*SI Appendix*, Fig. S4*B*). After store depletion using 1 μM TG, STIM1-Nterm-WT constructs showed increased FRET values, representing homomerization of N-terminal fragments, whereas constructs containing the TM-domain (aa200 to 233) alone, did not exhibit any detectable FRET values (*SI Appendix*, Fig. S4*A*). Unlike full-length STIM1-WT proteins, which form stable protein puncta after $Ca^{2+}$ stores have been depleted (Fig. 3*A*), STIM1-Nterm proteins retained their reticular distribution without exhibiting any clearly visible cluster formation, as previously described (*SI Appendix*, Fig. S4*B*) (25, 50). Engineering

these basic constructs with α7- and α9-mutations yielded similar low starting FRET values as the corresponding WT STIM1-Nterm form (*SI Appendix*, Fig. S4*A*). After TG treatment, cells expressing α9-mutated proteins just depicted a moderate increase in FRET after store depletion that was significantly smaller than the one determined for WT. Instead, α7-mutants maintained the low starting FRET values throughout the whole-time course (*SI Appendix*, Fig. S4*A*).

Considering the structural data of the luminal EF-SAM domain, we showed that multimerization of α7 and α9 EF-SAM mutants is compromised despite a lower $Ca^{2+}$ binding affinity of the α7-mutant. Given that the α7-residues are situated opposite to the EF-hand motif, a drop in $Ca^{2+}$ binding affinity, as shown by the dramatically lower midpoint of temperature denaturation of the α7-mutant, would suggest a destabilization of the SAM domain. Congruently, live-cell TIRF measurements of STIM1 α7- and α9-mutants largely lacked cluster formation upon ER-$Ca^{2+}$ store depletion. Hence, these experiments of the STIM1-α7 SAM region, point to a dual role in i) stabilization of the resting state and ii) multimerization of the luminal STIM1 domain.

**Orai1 Coexpression Partially Restores the Clustering Ability of Multimerization Mutants.** Having determined diminished cluster formation of both SAM mutants alone, we aimed to investigate the impact of the Orai1 channel on STIM1 puncta formation. Therefore, we conducted an analogous TIRF approach as depicted in Fig. 3 but coexpressed Orai1-YFP together with α7- and α9-mutants. Orai1 displayed a diffuse distribution in the PM, whereas STIM1 showed directed movement over the ER-membrane at resting cell conditions (Fig. 5*A*, Orai1 green, STIM red; Movie S9). After ER-$Ca^{2+}$ store depletion using CPA, STIM1-WT together with Orai1 formed immobile, stable clusters with an increased intensity and puncta area for both CRAC channel components at the PM (Fig. 5 *A* and *B* and *SI Appendix*, Figs. S4 *C* and *D* and S5 *A* and *B* and Movie S9). Instead, coexpression of STIM1-α7- or STIM1-α9-mutants together with Orai1, already resulted in a slightly increased number and intensity of puncta for both proteins even at resting conditions (Fig. 5*B* and *SI Appendix*, Fig. S4*C* and Movies S10 and S11). Particularly STIM1-α7 coexpression with Orai1 resulted in preformed clusters together with higher mean puncta area size and intensity even at resting cell conditions with modest increases upon ER-$Ca^{2+}$ store depletion (Fig. 5*B* and *SI Appendix*, Figs. S4 *C* and *D* and S5 *A* and *B* and Movie S10). Indeed, the number of resting-state STIM1-α7- and -α9-mutant puncta did not reach the values observed for STIM1-WT clusters upon store depletion. Also, the puncta intensity remained significantly lower for both mutants with a reduced number of clusters compared to WT after CPA treatment (Fig. 5*B* and *SI Appendix*, Fig. S4*C*). Monitoring of Orai1 cluster intensity was clearly dependent on the coexpression of STIM1-WT, STIM1-α7-, or -α9-mutants and followed their trend of puncta formation (*SI Appendix*, Fig. S5 *A* and *B*).

Together, these data strongly indicate that Orai1 is able to partially compensate the inhibitory effect of α7- and α9-mutants on cluster formation, most likely due to the physical interaction between STIM1 and Orai1 (48). While coexpression of STIM1-α7- and α9-mutants together with Orai1 can partially regain cluster formation, the number and intensity of clusters are still reduced compared to STIM1-WT.

**SAM α7 and α9 Multimerization Mutants Modulate SOCE and the Store-Operated $Ca^{2+}$ Oscillation Profile.** Having identified that cluster formation of STIM1-α7 and -α9 multimerization mutations is partially regained in the presence of Orai1, we asked how these mutants would affect the activation of Orai1 channels. To assess the activation kinetics of CRAC currents ($I_{CRAC}$), we performed electrophysiological measurements where CFP-Orai1 was expressed together with YFP-STIM1 or the respective mutants. To deplete cellular ER-$Ca^{2+}$ stores in clamped single cells, the slow $Ca^{2+}$ chelator EGTA was added to the pipette solution. Patch-clamp recordings conducted in the whole-cell configuration resulted in typical delayed $I_{CRAC}$ activation with a maximum current reached after ~200 s for STIM1-WT and Orai1 (Fig. 5*C*). Instead, cells expressing STIM1-α7- and α9-mutants exhibited significantly decreased maximum currents compared to WT (Fig. 5*C* and *SI Appendix*, Fig. S6*A*). Current-voltage relationships of maximum currents yielded similar $Ca^{2+}$-selective inward rectifying currents for STIM1-WT and both mutants upon coexpression with Orai1 (*SI Appendix*, Fig. S6*B*). Right after whole-cell break-in, cells expressing STIM1-α7 and Orai1 yielded a small constitutive current, which is in line with previously observed precluster formation upon coexpression of Orai1, its shifted quaternary structure and decreased $Ca^{2+}$ affinity (Figs. 4 *B*, *E*, *G*, and *I* and 5*C*). Additionally, $Ca^{2+}$ imaging experiments using Fura 2 yielded significantly decreased SOCE for both mutants after store depletion compared to STIM1-WT when expressed in S1/S2 dKO cells, supporting the results obtained in patch-clamp experiments (*SI Appendix*, Fig. S6*C*).

To further investigate the small constitutive activity of STIM1-α7, we also performed STIM1-Orai1 FRET experiments using S1/S2 dKO cells. In fact, in the absence of external stimulation, cells expressing STIM1-α7-CFP and Orai1-YFP resulted in higher starting FRET values than those expressing STIM1-WT or STIM1-α9 (*SI Appendix*, Fig. S6*D*). Both mutants responded with increased FRET values after treatment with TG but did not reach WT-like levels at the end of the experiment in line with diminished Orai1 activation (*SI Appendix*, Fig. S6*D*). Also, the constitutive yet small $Ca^{2+}$ influx observed during patch-clamp measurements and resting-state interactions apparent in FRET-based investigations upon STIM1-α7 and Orai1 coexpression, correlates with the preclustered localization at resting cell conditions monitored by TIRF microscopy (Fig. 5*A* and *SI Appendix*, Fig. S6*D*). In order to investigate the regaining effect of Orai1 on our identified mutants, we performed C-terminally labeled STIM1 homomerization experiments in the presence of mCherry-Orai1. The results clearly support the effect and showed increasing FRET values after TG treatment. Also, FRET values for the α7-mutant were increased already under resting state conditions and α9-mutants resulted in TG-treated end FRET values comparable to STIM1-WT (*SI Appendix*, Fig. S6*E*).

To study how luminal STIM1 multimerization mutants influence physiologically relevant SOCE signals, we induced $Ca^{2+}$ oscillation by receptor stimulation with low (5 μM) and high (100 μM) Carbachol (CCh), which acts as agonist for muscarinic receptors. High CCh concentration (100 μM) induced transient ER-$Ca^{2+}$ depletion followed by a characteristic subsequent $Ca^{2+}$ oscillation profile in HEK293 cells (Fig. 5 *D* and *E*). Upon treatment, cells can be categorized into three distinct groups based on their $Ca^{2+}$ oscillation profile, including i) $Ca^{2+}$ release–only events (named Release), ii) $Ca^{2+}$ oscillations that return to baseline between two $Ca^{2+}$ peaks (Baseline), or iii) oscillations with an elevated $Ca^{2+}$ plateau (Osc-elev) (Fig. 5 *E*, *Left*). Considering, untransfected control cells stimulated with 100 μM CCh, 21% depicted only a single $Ca^{2+}$ release event, 42% showed baseline oscillations and 37% displayed oscillations with an elevated plateau phase (Fig. 5*E*). Similar results to untransfected control cells could be observed for cells overexpressing STIM1-WT (release ~24%, baseline ~42%, and Osc-elevated ~35%) (Fig. 5*E*). While the proportion of cells expressing the STIM1-α7-mutant

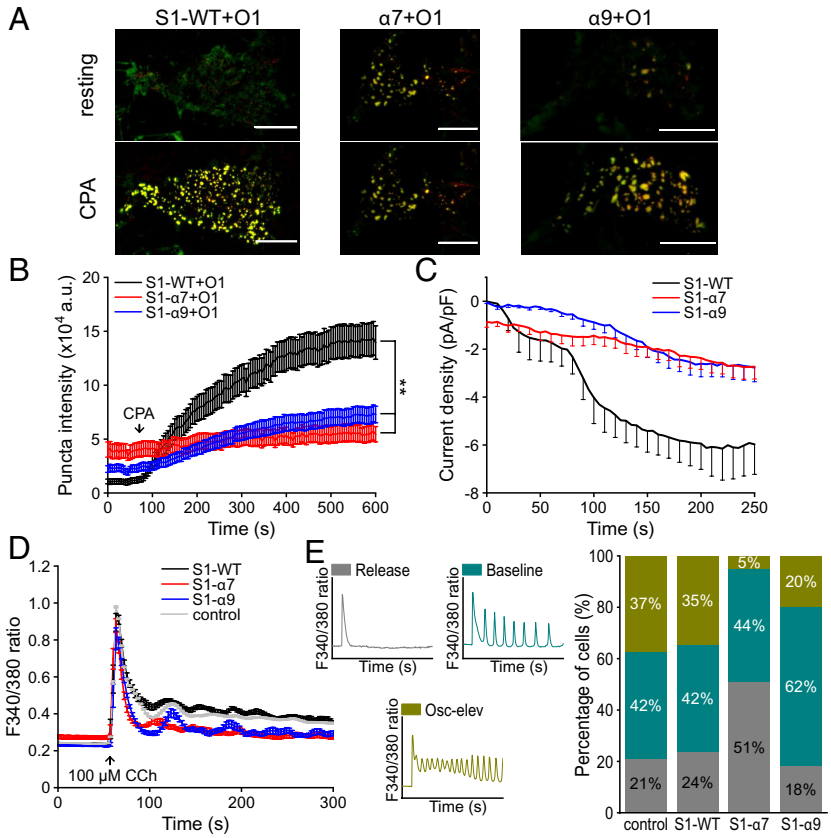


**Fig. 5.** Effects of N-terminal STIM1-α7 and -α9 activation on functional $Ca^{2+}$ signaling upon Orai1 overexpression. (*A* and *B*) Representative TIRFM images (*A*) and (*B*) time course of TIRF experiments representing increasing total cumulative STIM1 puncta intensity per cell after addition of 25 μM CPA (added at 60 s time point) in HEK293 cells expressing CFP-STIM1-WT (n = 68), STIM1-α7 (n = 49), and STIM1-α9 (n = 73) together with Orai1-YFP. In (*A*) CFP-STIM1 proteins depicted in red and Orai1-YFP in green at resting state (*Upper*) and after treatment with 25 μM CPA (*Lower*). (*C*) Time course of whole-cell patch-clamp recordings showing inward currents at −74 mV activated by passive store depletion of HEK293 cells by 20 mM EGTA in the pipette solution. HEK293 cells were coexpressing CFP-Orai1-WT together with YFP-STIM1-WT (n = 17), STIM1-α7 (n = 13), or STIM1-α9 (n = 14). (*D*) Time course of Fura 2 measurements in HEK293 cells overexpressing CFP-STIM1-WT (n = 493) STIM1-α7 (n = 185), STIM1-α9 (n = 312), or untransfected cells (control) (n = 1,936) upon stimulation using 100 μM Carbachol (CCh) in 1 mM $Ca^{2+}$ containing solution. (*E*) Data presented for different intracellular $Ca^{2+}$ $[Ca^{2+}]_i$ patterns (Release only in gray, baseline oscillations turquoise, and elevated oscillations olive) are shown representatively (*Left*). Bar graphs indicate the proportion of cell population displaying these various patterns of $[Ca^{2+}]_i$ changes in HEK293 cells overexpressing CFP-STIM1-WT (n = 486) STIM1-α7 (n = 118), STIM1-α9 (n = 238), or untransfected cells (control) (n = 1,836) upon stimulation using 100 μM Carbachol (CCh) in 1 mM $Ca^{2+}$ containing solution.

subserving baseline $Ca^{2+}$ oscillations were similar to STIM1-WT, a considerably reduced fraction of 5% of HEK293 cells showed $Ca^{2+}$ oscillation with an elevated plateau phase (Fig. 5*E*). Consequently, with ~51%, the majority of STIM1-α7-mutant expressing cells were of the release-only type (Fig. 5*E*). For HEK293 cells expressing STIM1-α9 mutated proteins, again a decrease in the fraction of cells exhibiting $Ca^{2+}$ oscillation with an elevated plateau was observed together with a small increase in baseline oscillations (62%) (Fig. 5*E*).

Treatment of α7- and α9-mutants with 5 μM CCh led to a similar trend in the oscillation profiles as observed for 100 μM CCh (*SI Appendix*, Fig. S6*F*). Yet, for the STIM1-α7-mutant, the proportion of cells only depicting a single $Ca^{2+}$ release event further increased from 51% to 70% upon switching to 5 μM CCh (Fig. 5*E* and *SI Appendix*, Fig. S6*G*). Instead, treatment of cells expressing STIM1-α9-mutant with the lower concentration yielded fewer cells that exhibited $Ca^{2+}$ oscillations with an elevated plateau phase (Fig. 5*E* and *SI Appendix*, Fig. S6*G*). Additionally, we also performed oscillation experiments in S1/S2 dKO cells. Unlike the dKO-control cells which only display 100 μM CCh-stimulated intracellular $Ca^{2+}$ release, dKO expressing STIM1-WT displayed sustained $Ca^{2+}$ oscillations (*SI Appendix*, Fig. S6*H*). In contrast, S1-α7- and α9-mutants showed similar characteristics as that of control cells and displayed only $Ca^{2+}$ release events (*SI Appendix*, Fig. S6*H*).

These functional experiments show that STIM1 multimerization mutants do not completely abolish $Ca^{2+}$ signaling of Orai1, but rather modulate the $Ca^{2+}$ oscillations profile, in line with previously presented electrophysiological and $Ca^{2+}$ imaging data.

**The α9 Single Multimerization Mutation L179A Takes on Central Role.** The data obtained for α7 and α9 triple- and double-alanine mutants, respectively, prompted us to find out whether a single- or double-point mutation would also be capable of altering STIM1 functions. Thus, we assessed $I_{CRAC}$ in HEK293 cells expressing individual YFP-STIM1-α7 single- or double-point alanine mutant combinations together with CFP-Orai1 in patch-clamp recordings. While $I_{CRAC}$ from single point mutants resulted in comparable currents as STIM1-WT, the F154A-R155A double mutant resulted in small constitutively active currents that could not further be stimulated by ER-store depletion (*SI Appendix*, Fig. S7*A*). In line, the F154A-R155A double mutant showed impaired STIM1 homomerization together with STIM1-Orai1 FRET measurements using S1/S2 dKO cells similar to results from the α7-mutant (triple). In addition, STIM1 homomerization was also partially impaired in F154A-K156A double mutants and patch clamp experiments yielded similar low activation like the α7-mutant, while all other STIM1-α7-mutants (single/double) yielded STIM1-WT-like values (*SI Appendix*, Fig. S7 *A*, *C*, and *E*).

We conducted analogous patch clamp and FRET experiments with α9 single mutants. Again, the individual STIM1-V178A mutation depicted results similar to those of STIM1-WT (*SI Appendix*, Fig. S7 *B*, *D*, and *F*). Intriguingly, the single point mutant L179A largely resembled the α9 double-alanine mutation time course. Specifically, when coexpressed with Orai1, STIM1-L179A yielded significantly decreased $I_{CRAC}$ currents in comparison to STIM1-WT (*SI Appendix*, Fig. S7*B*). In addition, homomerization of STIM1-L179A derived from FRET measurements was significantly reduced, exhibiting a comparatively small transient increase in FRET signals upon store depletion with TG (*SI Appendix*, Fig. S7*D*). In line with these observations, the number of clusters formed by STIM1-L179A increased only slightly after TG treatment and did not reach WT levels (*SI Appendix*, Fig. S7 *G* and *H*). The additional coexpression of Orai1 regained the number of STIM1-L179A clusters, still not completely restoring the analogous STIM1-WT cluster quantity (*SI Appendix*, Fig. S7 *G* and *H*). Evaluation of STIM1-Orai1 FRET after TG treatment, portrayed no significant differences between WT and the L179A mutant

(*SI Appendix*, Fig. S7*F*). Taken together, these experiments determined that among the five positions studied, residue L179 plays a key role for the ER-luminal STIM1 multimerization.

**Multimerization Mutations Decrease Cluster Formation Even in the Presence of a Defective EF-Hand.** As mentioned previously, the STIM1-α7-mutant exhibited in addition to its defect in N-terminal multimerization and cluster formation, a decreased $Ca^{2+}$ binding affinity in biochemical experiments. As ER-luminal STIM1 interactions are induced by store depletion events, we investigated whether diminished N-terminal multimerization of α7- and α9-mutants is still preserved upon completely preventing the cEF-hand from $Ca^{2+}$-binding. According to structural data, the aspartic acid at position 76 is an essential residue to coordinate a single $Ca^{2+}$ ion (21, 22, 30). A D76A mutation has been shown to disturb the $Ca^{2+}$ sensitivity of the cEF-hand domain, consequently simulating store depletion and switching the protein into a constitutively active state (9, 51, 52). Therefore, we combined α7 and α9 STIM1-mutants with the EF-hand mutation D76A (D76A-α7, D76A-α9). Consistently, a high number of STIM1-D76A clusters were already observed under resting cell conditions in our confocal fluorescence measurements with a slight further increase after treatment with TG (Fig. 6 *A* and *B*). In contrast to this strongly activating effect of STIM1-D76A alone, combining STIM1-D76A with the α7 or α9 alanine substitutions largely diminished the numbers of preformed clusters during resting state conditions, which only marginally increased after ER depletion (Fig. 6 *A* and *B*). Coexpression of Orai1 could partially regain cluster formation in the store-replete state in the case of both EF-hand-SAM domain combination mutations (*SI Appendix*, Fig. S8 *A* and *B*).

In correlation with observed preformed STIM1-D76A clusters, patch clamp experiments upon coexpression of STIM1-D76A and Orai1 showed constitutively active currents, as calculated after whole-cell break-in, independent of store depletion by 20 mM EGTA in the pipette solution. When Orai1 was overexpressed together with STIM1-mutants, analogous patch clamp experiments exhibited reduced constitutive activation for both mutants. In addition, the constitutive currents of STIM1-D76A-α7 were significantly reduced compared to those of the STIM1-D76A single mutant (Fig. 6*C* and *SI Appendix*, Fig. S8*C*).

The results of these experiments clearly separate $Ca^{2+}$ binding affinity and multimerization efficiency. D76A combinations reveal that interferences in the α7 and α9 N-terminal multimerization sites result in diminished cluster formation and $I_{CRAC}$ even when the EF-hand lacks the ability to bind $Ca^{2+}$, underlining the importance of the N-terminal domain in the multimerization process for STIM1 activation.

**Monitoring STIM1 C-Terminal Activation in the Presence of Luminal Multimerization Mutations.** The cluster formation recovery of STIM1 multimerization mutants in the presence of Orai1 suggests that the two mutants at least transiently switch into an active configuration upon ER-$Ca^{2+}$ store depletion. An active configuration of STIM1 involves CAD to be accessible for interactions with Orai1 channels in the PM. In its resting state, CAD is masked by direct binding to CC1, forming a tightly packed configuration (36, 37, 42, 43, 50, 53). Structural changes in this C-terminal domain, resulting in an active STIM1 configuration, are mediated by luminal multimerization which triggers CC1-CC1 coiled-coil zip formation, forcing the CAD apex to move away from the ER-membrane (35–37, 45, 50, 54). The uncoupling of CAD from CC1 after store depletion can be visualized as previously shown by our and other groups, using a two-component system of STIM1 fragments with one construct including a stop-codon after CC1 (STIM1-CC1, aa1-343) while the second component represents a soluble CAD (aa344 to 449) alone (*SI Appendix*, Fig. S8*D*) (30, 36). We monitored CFP-tagged STIM1 CC1 truncations and YFP-tagged CAD by colocalization analysis in confocal fluorescence experiments. During resting state, tight interaction between STIM1-1-343-WT and CAD yielded a high colocalization Pearson correlation coefficient (R-factor), which decreased after store depletion with TG, consistent with the dissociation of CAD away from CC1 (Fig. 6*D*). As constitutively active STIM1 control, we engineered the CC1-containing component with a H72R mutation, which is well established to destabilize the hydrophobic pocket of STIM1 proteins (30). In the present study and our previous work, we observed low colocalization of this mutant-containing constellation, regardless of TG-mediated store depletion (Fig. 6*D*) (30). Next, we assessed the impact of α7- and α9-mutants on the mechanism of C-terminal STIM1 activation using the same two-component approach. The STIM1-α9 CC1 fragment yielded a similar high interaction with CAD as observed for STIM1-WT without external stimulation. Upon $Ca^{2+}$ store depletion, colocalization between STIM1-1-343-α9 and CAD decreased to an almost similar extent as was observed for WT, indicating WT-like C-terminal activation triggered via the loss of $Ca^{2+}$ from the EF-hand domain (Fig. 6*D*). The colocalization between STIM1-1-343-α7-mutant and CAD started with a decreased colocalization that did not change upon TG treatment. These observations on the α7-mutant apparently point to an already preactivated state that cannot be activated further, again in accordance with live-cell experiments and biochemistry data (Fig. 6*D*). The experiments on the α9-mutant indicate that besides a largely impaired N-terminal multimerization upon ER-$Ca^{2+}$ store depletion, the interference in the STIM1 multimerization site still extends to the CAD domain, at least to a certain point. This is well in line with partial rescuing effects seen upon coexpressing Orai1 due to physical interactions of both STIM1 and Orai1 proteins.

**STIM1 Cluster Formation Induced by a Gain of Function Mutation in the C Terminus Is Not Reversed by α7 or α9 SAM Mutations.** Finally, we investigated whether constitutively formed STIM1 clusters induced by C-terminal modifications are diminished by luminal STIM1 multimerization mutants. For this, we harnessed the well-characterized Stormorken disease–causing STIM1-R304W mutation located in CC1. Structural investigations of the Stormorken mutant have shown that the arginine to tryptophan substitution at amino acid position 304 at the end of CC1α2 causes an extended rigid CC1α2 helix, leading to reduced flexibility between CC1α2 and CC1α3, causing CC1 dimerization and finally full activation of STIM1 (37, 44, 55, 56). As expected, we observed store-independent cluster formation for cells expressing STIM1-R304W mutants (Fig. 6 *E* and *F*). Unlike previously described data on D76A-α7 and D76-α9, combination of R304W with either α7- (R304W-α7) or α9- (R304W-α9) mutations, revealed similarly high puncta formation as STIM1 R304W under resting state conditions (Fig. 6 *E* and *F*). In addition, currents recorded upon coexpressing STIM1-R304W with Orai1, yielded constitutive activity. In support of the data on puncta formation, similar strong constitutive Orai1 currents were retained also upon coexpression with STIM1-R304W-α7 or STIM1-R304W-α9 (*SI Appendix*, Fig. S8 *E* and *F*).

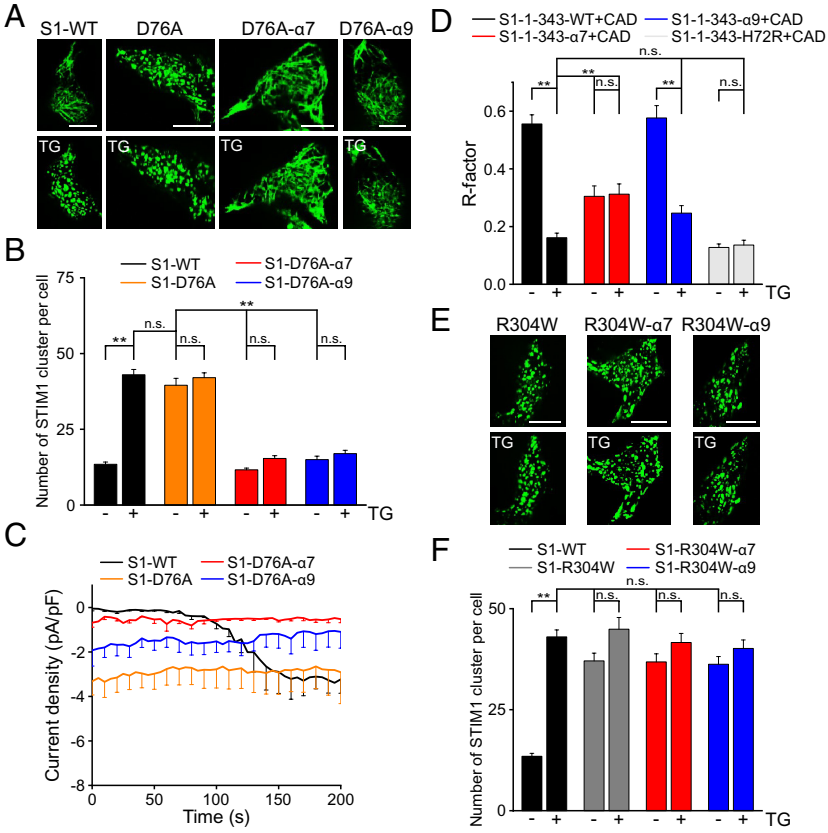


**Fig. 6.** Functional effects of SAM mutants on constitutively active STIM mutants. (*A* and *B*) Confocal fluorescence images (*A*) and average STIM1 clusters per cell (*B*) for HEK293 cells expressing CFP-STIM1-WT (rest: n = 81; TG: n = 67), CFP-STIM1-D76A (rest: n = 19; TG: n = 31), CFP-STIM1-D76A-α7 (rest: n = 31; TG: n = 49), and CFP-STIM1-D76A-α9 (rest: n = 40; TG: n = 39) at resting conditions and after addition of 1 μM TG. (*C*) Time course of whole-cell patch-clamp experiments showing inward currents at −74 mV activated by passive store depletion of HEK293 cells with 20 mM EGTA in the pipette solution. HEK293 cells were coexpressing CFP-Orai1-WT and YFP-STIM1-WT (n = 4), STIM1-D76A (n = 7) STIM1-D76A-α7 (n = 5) or STIM1-D76A-α9 (n = 5). (*D*) Bar graphs representing Pearson correlation value (R-factor) of CFP-STIM1-1-343 and YFP-CAD colocalization experiments in HEK293 cells expressing N-terminally tagged CFP-STIM1-WT (rest: n = 37; TG: n = 40), STIM1-α7 (rest: n = 34; TG: n = 29), STIM1-α9 (rest: n = 39; TG: n = 38), and STIM1-H72R (rest: n = 27; TG: n = 36) in dependence of 1 μM TG treatment. (*E* and *F*) Confocal fluorescence microscopy images (*E*) and mean values of number of puncta per cell (*F*) before and after addition of 1 μM TG for HEK293 cells expressing CFP-STIM1-WT (rest: n = 81; TG: n = 67), CFP-STIM1-R304W (rest: n = 29; TG: n = 38), CFP-STIM1-R304W-α7 (rest: n = 33; TG: n = 38), and CFP-STIM1-R304W-α9 (rest: n = 37; TG: n = 32).

Based on these results, manipulation of C-terminal domains, in this case by inserting the Stormorken disease causing R304W mutation, force multimerization of the protein, switching the protein into an active configuration and overruling the inhibitory effect of SAM-α7- and -α9-mutants. Clearly, the luminal multimerization sites need to be dynamic in order to switch between resting monomeric and activated multimeric state, hence a strong C-terminal active configuration is not affected by α7 and α9 mutations. This again strengthens the fact, that STIM1 activation is a very sensitive system, which can be pushed either to an inactive or active configuration by manipulations of different compartments and binding partners proven by D76A and R304W combinations and also seen through the coexpression of Orai1 proteins.

## Discussion

In this study, we identified crucial residues in the SAM domain essential for EF-SAM luminal multimerization and their effect on STIM1 activation. Through MD simulations that mimic ER-$Ca^{2+}$ store depletion, we highlighted the importance of the α7 segment and the adjacent region near α9 for STIM1 multimerization. Specifically, we found key interactions at residues F154, R155, K156, V178, and L179 and showed that mutations in these regions significantly reduce STIM1 puncta formation, affect peptide assembly into multimers and decrease SOCE. Notably, mutations impaired $Ca^{2+}$ oscillations under agonist stimulation, indicating a vital role in pacing $Ca^{2+}$ dynamics. This reveals how modifications of the MD-predicted STIM1 multimerization positions can affect Orai1 channel activation and $Ca^{2+}$ entry regulation.

Here, we identified specific residues within distinct SAM regions, in α7 and its adjacent region near α9, crucial for STIM1 multimerization both in vitro and in vivo. Notably, the three key residues in α7 are situated within a previously proposed SAM dimer forming region, spanning positions V134-L157, which has been implicated in the stabilization of STIM1 dimer formation via hydrophobic and aromatic interactions with α6 and α7 (32). Furthermore, these SAM regions displayed resistance to chymotrypsin digestion, indicating significant structural stability (32). The SAM domain, known for its role in multimerization across various protein, was corroborated by size-exclusion chromatography (SEC) coupled with multiangle light scattering (MALS) and electron microscopy experiments, which revealed the presence of dimers and higher order oligomers of purified luminal STIM1 upon $Ca^{2+}$ depletion (22, 57). In an alternative approach, an engineered construct combining the human STIM1 EF-SAM domain with a bacterial coiled-coil (GrpE) to mimic the first coiled-coil domain of STIM1 displayed only minimal loss in α-helix content upon $Ca^{2+}$ removal, suggesting a transition to a second structured conformation involving neither significant unfolding nor multimerization (58). In this regard, hydrogen to deuterium exchange at backbone amides of the luminal STIM1 peptide domain did not substantially change in dependence of $Ca^{2+}$ depletion. This has been particularly observed for α7 and α9 containing peptides (58). Reconciling these data with the current findings, one might suggest that α7 and α9 residues that become transiently accessible during ER $Ca^{2+}$ depletion would again be buried during di/multimerization. Consistently, the luminal STIM1 dimer investigated in our MD simulation study retained largely structured α-helices, reinforcing the importance of the SAM-mediated multimerization region in STIM1 function.

Based on SAM mediated structure-based oligomerization models and sequence alignments, several individual point mutations in STIM1 α7, α9, and α10 have previously been investigated but did not reveal drastic changes compared to the WT quaternary structure (22). Interestingly, among the mutations investigated in a previous work, the substitution of L179 to a positively charged arginine, was

unable to change multimerization behavior (22). Instead, our STIM1-L179A mutation, which retains the hydrophobic characteristic at this position, but depicts a much smaller side-chain, largely affected the STIM1–STIM1 interaction properties either alone or combined with V178A. It is of note that L179 is, among the residues investigated here, the most conserved amino acid across different species. Remarkably, out of the five investigated residues, only the STIM1 L179A single point mutant largely affected STIM1 clustering and yielded significantly reduced store-operated $Ca^{2+}$ currents upon coexpression with Orai1. Still, we cannot rule out that the evaluated point mutations imposed allosteric effects on protein functions or stabilized interactions of EF-SAM with the ER-membrane or with non-STIM proteins; however, we believe that the determined key residues are an ideal starting point for more detailed analysis of the luminal multimerization domain.

Intriguingly, Orai1 as well as the STIM1 gain of function R304W mutation are able to restore the ability of the N-terminal mutants to form puncta and establish $Ca^{2+}$ currents over the plasma membrane, at least in parts. Also, the overexpression of STIM1-WT proteins together with STIM1-α7 and STIM1-α9 can partially switch the protein back to functional luminal multimerization, suggesting that heteromers partially reestablish STIM1 function (*SI Appendix*, Fig. S9 *A* and *B*). This points to a graded shift in the STIM1 activation process that strictly depends on Orai1 and C-terminal STIM1 interactions. The stronger effect of C-terminal STIM1-R304W compared to STIM1-α7 and STIM1-α9 multimerization impeding mutations is in line with a fine-tuned balance between luminal assembly and disassembly required for store-operated activation and to return to its resting state.

The fact that the STIM1-α7-mutant decreased both the $Ca^{2+}$ binding affinity but also multimerization of purified EF-SAM peptides and in live-cell experiments points to a dual role of α7-residues in resting and multimerized ER-luminal STIM1. The lower $Ca^{2+}$ binding affinity of the α7-mutant was determined by a dramatically lower midpoint of temperature-dependent denaturation compared to WT luminal STIM1 peptides. The three α7-residues are located on the opposite side of the proteins as the EF-hand motifs, therefore a lower $Ca^{2+}$ binding affinity must result from destabilizing of the SAM domain. Such a double functional role of α7 assumedly leads to small constitutive $Ca^{2+}$ currents and minor puncta formation in the presence of overexpressed Orai1 at resting cell conditions. A recently published MD paper, which uncovered the temperature sensitivity of the noncanonical EF-hand domain, also suggested a stabilizing role of the SAM domain, especially via contacts between F108 (noncanonical EF-hand) and residues located at α10 (SAM), in the resting state and a transient F108 side-chain exposure in the partially unfolded $Ca^{2+}$-unbound/temperature-activated state potentially promoting EF-SAM di/multimerization (39). We also identified pronounced contact sites at this α3 region including F108 in our MD simulation dimerization approach as an important region for N-terminal di/multimerization. Such a double functional role of EF/SAM domains that stabilize both the resting but also the multimerization state of STIM1, as observed for α7, may promote switching between these two configurations. Further work is needed to fully understand this double function of EF/SAM key residues and in this regard address the importance of F108 in the di/multimerization process as recently proposed (39).

Disturbance of the $Ca^{2+}$ binding sensitivity introduced through the prominent D76A mutation or collapsing of the hydrophobic cleft integrity resulting from mutations including H72R, F108I, or E87Q has been shown to result in unfolding processes especially at regions involving the α2 and α3 of N-terminal STIM1 monomers (30, 31, 39). In comparison to partially unfolded STIM1 EF-hand mutants, like STIM1-D76A, cluster formation in both STIM1-α7- and STIM1-α9-mutants is reduced, as their ER-located multimerization is significantly hampered. Upon store depletion, the impaired multimerization STIM1-α7-mutant also significantly decreased maximum $Ca^{2+}$ currents. STIM1-α7- as well as α9-mutants, are able to interfere with endogenous $Ca^{2+}$ oscillations, likely due to formation of heteromeric endogenous STIM1-WT with STIM1-α7- and -α9-mutants. These heteromers are likely expected to form dimers via the C-terminal intermolecular (swapped) CC1-CAD configuration (37, 54).

Based on our results in combination with previous work, we expand insights into structural changes during the initial STIM1 activation cascade. Built on our MD simulations, functional and structural data, we depicted an activation cascade highlighting the importance of structural unfolding and di/multimerization of distinct regions of the luminal EF-SAM segment, initially triggered by the release of $Ca^{2+}$ from the cEF-hand domain (20, 30–32). Our MD results strongly support the notion that α2 and α3 helical unfolding of EF-SAM is necessary for di/multimerization, as we could hardly detect any interactions occurring during MD simulations under $Ca^{2+}$ saturating conditions. In the starting resting state configuration, the ER-luminal STIM1 domains are monomeric and clearly separated. This resting state configuration is stabilized by the C-terminal CC1-CAD interaction (17, 37, 43). The initial α2 and α3 helical unfolding expands the dimensions of the luminal STIM1 and favors an enhanced capture radius that induces first binding events between the so far monomeric luminal STIM1 domains. The fact that ER-luminal STIM1-α7 not only affected cluster formation but also decreased the $Ca^{2+}$ binding affinity suggests a dual role of the α7 domain both to stabilize the resting configuration and also enable luminal STIM1 multimerization. A similar functional role may also apply to the nEF-hand (30, 31, 39). As we observed dynamic dimer forming interactions of $Ca^{2+}$-free unfolded ER-luminal STIM1 monomers, we presume that several amino acids are required to maintain ER-luminal multimerization after the loss of $Ca^{2+}$. Multimerization in the ER-luminal parts conveys signals via the TM helix to CC1 in the cytosolic part of STIM1, inducing CC1 zipping hand in hand with the detachment of CAD (CC3) further strengthening ER-luminal STIM1 multimerization together with CC3 homomerization, finally leading to solid STIM1 cluster formation (35, 37, 38, 43, 54).

In summary, we here identify regions located in α7 and the adjacent region near α9 of the SAM domain, which are crucial for facilitating stable STIM1 multimerization. This information provides mechanistic insights into intermediate luminal STIM1 activation states beginning with partial unfolding and sequential intermolecular interaction cascades between STIM1 proteins.

## Materials and Methods

Cell culture and transfection for HEK293 cells and S1/S2 CRISPR dKO cells transfected with STIM1 and Orai1 plasmids used is described in *SI Appendix*. Live cell experiments including confocal microscopy imaging, calcium imaging, electrophysiological recordings, and TIRF microscopy imaging are extensively described in *SI Appendix*. Molecular dynamics simulations used the crystal structure of the *h*STIM luminal domain (PDB ID:2K60) (22). All information on modeled domains, configurations of domains, force field, molecular dynamics simulations, and data visualization are extensively described in *SI Appendix*. Protein expression and purification of constructs encompassing *h*STIM1 EF-SAM (NM003156) residues 58 to 201 of wild-type and mutants (WT), together with analysis by size exclusion chromatography with in-line multiangle light scattering and far-UV circular dichroism spectroscopy are also described in *SI Appendix*. All statistical analysis tests using OriginPro 2022 (OriginLab Corporation), significance tests, and data presentations are described in *SI Appendix*.

**Data, Materials, and Software Availability.** All study data are included in the article and/or supporting information.

**ACKNOWLEDGMENTS.** We thank S. Buchegger for excellent technical assistance. This work was supported by the Austrian Science Fund (FWF) through projects P32778 to R.S., P32947 to M.F., T1190-B to R.L., P33283 and P34884 to C.R., NSERC 05239 to P.B.S. as well as D.B. was supported by the Czech Science Foundation (19-20728Y). Access to the National Grid Infrastructure Metacentrum and provided computational resources are gratefully acknowledged. Funding for work done by H.L.O., S.N., and S.C. was provided by NIDCR-Division of Intramural Research, NIH (Z01-DE00438-33) to I.A.

Author affiliations: [a]Institute of Biophysics, Johannes Kepler University Linz, Linz 4040, Austria; [b]Secretory Physiology Section, National Institute of Dental and Craniofacial Research, NIH, Bethesda, MD 20892; [c]Department of Physiology and Pharmacology, Western University, London, ON N6A5C1, Canada; [d]Department of Medical Physics and Biophysics, Medical University of Graz, Graz 8010, Austria; and [e]Department of Physics and Materials Science, Faculty of Science, Technology and Medicine, University of Luxembourg, Esch-sur-Alzette L1511, Luxembourg

Author contributions: M.S., H.L.O., S.N., P.B.S., I.A., C.R., R.L., D.B., and R.S. designed research; M.S., C.H., H.L.O., S.N., Q.T.L., M.F., H.G., S.B., S.C., L.M., L.A., D.B., and R.S. performed research; M.S., C.H., H.L.O., S.N., Q.T.L., M.F., H.G., S.B., T.S., M.N., I.F., D.B., and R.S. contributed new reagents/analytic tools; M.S., C.H., H.L.O., S.N., Q.T.L., H.G., L.M., P.B.S., D.B., and R.S. analyzed data; and M.S., H.L.O., S.N., C.R., P.B.S., I.A., R.L., D.B., and R.S. wrote the paper.

1. M. Brini, D. Ottolini, T. Cali, E. Carafoli, Calcium in health and disease. *Met Ions Life Sci.* **13**, 81–137 (2013).
2. M. J. Berridge, M. D. Bootman, H. L. Roderick, Calcium signalling: Dynamics, homeostasis and remodelling. *Nat. Rev. Mol. Cell Biol.* **4**, 517–529 (2003).
3. M. Prakriya, R. S. Lewis, Store-operated calcium channels. *Physiol. Rev.* **95**, 1383–1436 (2015).
4. J. W. Putney Jr., A model for receptor-regulated calcium entry. *Cell Calcium* **7**, 1–12 (1986).
5. S. M. Emrich, R. E. Yoast, M. Trebak, Physiological functions of CRAC channels. *Annu. Rev. Physiol.* **84**, 355–379 (2022).
6. S. L. Zhang *et al.*, STIM1 is a Ca2+ sensor that activates CRAC channels and migrates from the Ca2+ store to the plasma membrane. *Nature* **437**, 902–905 (2005).
7. S. Parvez *et al.*, STIM2 protein mediates distinct store-dependent and store-independent modes of CRAC channel activation. *FASEB J.* **22**, 752–761 (2008).
8. S. Feske *et al.*, A mutation in Orai1 causes immune deficiency by abrogating CRAC channel function. *Nature* **441**, 179–185 (2006).
9. J. Liou *et al.*, STIM is a Ca2+ sensor essential for Ca2+-store-depletion-triggered Ca2+ influx. *Curr. Biol.* **15**, 1235–1241 (2005).
10. J. Roos *et al.*, STIM1, an essential and conserved component of store-operated Ca2+ channel function. *J. Cell Biol.* **169**, 435–445 (2005).
11. M. M. Wu, J. Buchanan, R. M. Luik, R. S. Lewis, Ca2+ store depletion causes STIM1 to accumulate in ER regions closely associated with the plasma membrane. *J. Cell Biol.* **174**, 803–813 (2006).
12. L. Orci *et al.*, From the cover: STIM1-induced precortical and cortical subdomains of the endoplasmic reticulum. *Proc. Natl. Acad. Sci. U.S.A.* **106**, 19358–19362 (2009).
13. H. Grabmayr, C. Romanin, M. Fahrner, STIM proteins: An ever-expanding family. *Int. J. Mol. Sci.* **22**, 378 (2020).
14. R. M. Luik, B. Wang, M. Prakriya, M. M. Wu, R. S. Lewis, Oligomerization of STIM1 couples ER calcium depletion to CRAC channel activation. *Nature* **454**, 538–542 (2008).
15. J. Liou, M. Fivaz, T. Inoue, T. Meyer, Live-cell imaging reveals sequential oligomerization and local plasma membrane targeting of stromal interaction molecule 1 after Ca2+ store depletion. *Proc. Natl. Acad. Sci. U.S.A.* **104**, 9301–9306 (2007).
16. R. M. Luik, M. M. Wu, J. Buchanan, R. S. Lewis, The elementary unit of store-operated Ca2+ entry: Local activation of CRAC channels by STIM1 at ER-plasma membrane junctions. *J. Cell Biol.* **174**, 815–825 (2006).
17. M. Sallinger *et al.*, Activation mechanisms and structural dynamics of STIM proteins. *J. Physiol.* **602**, 1475–1507 (2023), 10.1113/JP283828.
18. M. Muik *et al.*, A cytosolic homomerization and a modulatory domain within STIM1 C terminus determine coupling to ORAI1 channels. *J. Biol. Chem.* **284**, 8421–8426 (2009).
19. X. Cai, Molecular evolution and functional divergence of the Ca(2+) sensor protein in store-operated Ca(2+) entry: Stromal interaction molecule. *PLoS One* **2**, e609 (2007).
20. M. Enomoto *et al.*, Coordination of a single calcium ion in the EF-hand maintains the off state of the stromal interaction molecule luminal domain. *J. Mol. Biol.* **432**, 367–383 (2020).
21. P. B. Stathopulos, G. Y. Li, M. J. Plevin, J. B. Ames, M. Ikura, Stored Ca2+ depletion-induced oligomerization of stromal interaction molecule 1 (STIM1) via the EF-SAM region: An initiation mechanism for capacitive Ca2+ entry. *J. Biol. Chem.* **281**, 35855–35862 (2006).
22. P. B. Stathopulos, L. Zheng, G. Y. Li, M. J. Plevin, M. Ikura, Structural and mechanistic insights into STIM1-mediated initiation of store-operated calcium entry. *Cell* **135**, 110–122 (2008).
23. X. Yang, H. Jin, X. Cai, S. Li, Y. Shen, Structural and mechanistic insights into the activation of Stromal interaction molecule 1 (STIM1). *Proc. Natl. Acad. Sci. U.S.A.* **109**, 5657–5662 (2012).
24. G. N. Huang *et al.*, STIM1 carboxyl-terminus activates native SOC, I(crac) and TRPC1 channels. *Nat. Cell Biol.* **8**, 1003–1010 (2006).
25. E. D. Covington, M. M. Wu, R. S. Lewis, Essential role for the CRAC activation domain in store-dependent oligomerization of STIM1. *Mol. Biol. Cell* **21**, 1897–1907 (2010).
26. C. Y. Park *et al.*, STIM1 clusters and activates CRAC channels via direct binding of a cytosolic domain to Orai1. *Cell* **136**, 876–890 (2009).
27. J. P. Yuan *et al.*, SOAR and the polybasic STIM1 domains gate and regulate Orai channels. *Nat. Cell Biol.* **11**, 337–343 (2009).
28. L. Zheng *et al.*, Auto-inhibitory role of the EF-SAM domain of STIM proteins in store-operated calcium entry. *Proc. Natl. Acad. Sci. U.S.A.* **108**, 1337–1342 (2011).
29. Y. Zhou *et al.*, The short N-terminal domains of STIM1 and STIM2 control the activation kinetics of Orai1 channels. *J. Biol. Chem.* **284**, 19164–19168 (2009).
30. R. Schober *et al.*, Sequential activation of STIM1 links Ca(2+) with luminal domain unfolding. *Sci. Signal* **12**, eaax3194 (2019).
31. M. Sallinger *et al.*, Luminal STIM1 mutants that cause tubular aggregate myopathy promote autophagic processes. *Int. J. Mol. Sci.* **21**, 4410 (2020).
32. Y. Furukawa *et al.*, Intrinsic disorder mediates cooperative signal transduction in STIM1. *J. Mol. Biol.* **426**, 2082–2097 (2014).
33. G. Y. Son *et al.*, STIM2 targets Orai1/STIM1 to the AKAP79 signaling complex and confers coupling of Ca(2+) entry with NFAT1 activation. *Proc. Natl. Acad. Sci. U.S.A.* **117**, 16638–16648 (2020).
34. K. P. Subedi, H. L. Ong, G. Y. Son, X. Liu, I. S. Ambudkar, STIM2 induces activated conformation of STIM1 to control Orai1 function in ER-PM junctions. *Cell Rep.* **23**, 522–534 (2018).
35. N. Hirve, V. Rajanikanth, P. G. Hogan, A. Gudlur, Coiled-coil formation conveys a STIM1 signal from ER lumen to cytoplasm. *Cell Rep.* **22**, 72–83 (2018).
36. N. Shrestha *et al.*, Mapping interactions between the CRAC activation domain and CC1 regulating the activity of the ER Ca(2+) sensor STIM1. *J. Biol. Chem.* **298**, 102157 (2022).
37. S. van Dorp *et al.*, Conformational dynamics of auto-inhibition in the ER calcium sensor STIM1. *Elife* **10**, e66194 (2021).
38. M. Fahrner, H. Grabmayr, C. Romanin, Mechanism of STIM activation. *Curr. Opin. Physiol.* **17**, 74–79 (2020).
39. A. Neamtu *et al.*, Molecular dynamics simulations reveal the hidden EF-hand of EF-SAM as a possible key thermal sensor for STIM1 activation by temperature. *J. Biol. Chem.* **299**, 104970 (2023), 10.1016/j.jbc.2023.104970.
40. B. Cui *et al.*, The inhibitory helix controls the intramolecular conformational switching of the C-terminus of STIM1. *PloS One* **8**, e74735 (2013).
41. J. Bohm *et al.*, Constitutive activation of the calcium sensor STIM1 causes tubular-aggregate myopathy. *Am. J. Hum. Genet.* **92**, 271–278 (2013).
42. M. Muik *et al.*, STIM1 couples to ORAI1 via an intramolecular transition into an extended conformation. *EMBO J.* **30**, 1678–1689 (2011).
43. M. Fahrner *et al.*, A coiled-coil clamp controls both conformation and clustering of stromal interaction molecule 1 (STIM1). *J. Biol. Chem.* **289**, 33231–33244 (2014).
44. P. Rathner *et al.*, Interhelical interactions within the STIM1 CC1 domain modulate CRAC channel activation. *Nat. Chem. Biol.* **17**, 196–204 (2021).
45. P. B. Stathopulos *et al.*, STIM1/Orai1 coiled-coil interplay in the regulation of store-operated calcium entry. *Nat. Commun.* **4**, 2963 (2013).
46. J. Pacheco, L. Dominguez, A. Bohorquez-Hernandez, A. Asanov, L. Vaca, A cholesterol-binding domain in STIM1 modulates STIM1-Orai1 physical and functional interactions. *Sci. Rep.* **6**, 29634 (2016).
47. Y. Zhou *et al.*, STIM1 gates the store-operated calcium channel ORAI1 in vitro. *Nat. Struct. Mol. Biol.* **17**, 112–116 (2010).
48. M. Muik *et al.*, Dynamic coupling of the putative coiled-coil domain of ORAI1 with STIM1 mediates ORAI1 channel activation. *J. Biol. Chem.* **283**, 8014–8022 (2008).
49. I. Frischauf *et al.*, Molecular determinants of the coupling between STIM1 and Orai channels: Differential activation of Orai1-3 channels by a STIM1 coiled-coil mutant. *J. Biol. Chem.* **284**, 21696–21706 (2009).
50. G. Ma *et al.*, Inside-out Ca(2+) signalling prompted by STIM1 conformational switch. *Nat. Commun.* **6**, 7826 (2015).
51. M. A. Spassova *et al.*, STIM1 has a plasma membrane role in the activation of store-operated Ca(2+) channels. *Proc. Natl. Acad. Sci. U.S.A.* **103**, 4040–4045 (2006).
52. S. L. Zhang *et al.*, Genome-wide RNAi screen of Ca2+ influx identifies genes that regulate Ca2+ release-activated Ca2+ channel activity. *Proc. Natl. Acad. Sci. U.S.A.* **103**, 9337–9362 (2006), 10.1073/pnas.0603161103.
53. Y. Zhou *et al.*, Initial activation of STIM1, the regulator of store-operated calcium entry. *Nat. Struct. Mol. Biol.* **20**, 973–981 (2013).
54. F. Horvath *et al.*, Swing-out opening of stromal interaction molecule 1. *Protein Sci.* **32**, e4571 (2023).
55. M. Fahrner *et al.*, A dual mechanism promotes switching of the Stormorken STIM1 R304W mutant into the activated state. *Nat. Commun.* **9**, 825 (2018).
56. T. H. Gamage *et al.*, A single amino acid deletion in the ER Ca(2+) sensor STIM1 reverses the in vitro and in vivo effects of the Stormorken syndrome-causing R304W mutation. *Sci. Signal* **16**, eadd0509 (2023).
57. C. A. Kim, J. U. Bowie, SAM domains: Uniform structure, diversity of function. *Trends Biochem. Sci.* **28**, 625–628 (2003).
58. A. Gudlur *et al.*, Calcium sensing by the STIM1 ER-luminal domain. *Nat. Commun.* **9**, 4536 (2018).